Aerodynamics of headsails: a review of measured surface pressures and expected flow fields

AERODYNAMICS OF HEADSAILS: A REVIEW OF MEASURED SURFACE PRESSURES AND EXPECTED FLOW FIELDS

Ignazio Maria Viola[1], i.m.viola@ed.ac.uk
Richard Flay[2], r.flay@auckland.ac.nz

Abstract. The general flow features observed on yacht sails can be predicted with well-established fluid dynamic theory. Headsails are thin wings with a sharp leading edge and thin-airfoil theory can predict the general flow and pressure fields around these sails. However, a closer look shows viscous flow features, such as the leading edge bubble, that cannot be modelled with inviscid flow and, indeed, cannot be predicted accurately with analytical fluid dynamics. Moreover, the available literature lacks of quantitative flow measurements (e.g. particle imaging velocimetry) and high-fidelity numerical simulations (e.g. wall-resolved large eddy simulations) on yacht sails due to the difficulties related to the high Reynolds numbers and the complex sails' geometries. Therefore there is limited knowledge of the viscous flow field near sails. Here we provide a detailed description of the pressure distributions measured in a wind tunnel on model-scale headsails and we describe the expected flow field with analogies with other viscous fluid flows. We show that while the general pressure distribution trend is dominated by potential flow, the viscous flow features have a significant effect on the pressure distributions near the leading and trailing edges. In particular, we propose that a long-type laminar separation bubble occurs at the leading edge while trailing edge separation may occur at high angles of attack; we discuss how these features vary with the sail geometry, the angle of attack, the Reynolds number and the turbulence level of the onset flow. We think that the proposed description of these flow features will enhance the interpretation of sail pressure distributions and, in turn, of the aerodynamic forces experienced by a sailing yacht.

1. INTRODUCTION

The flow field around upwind yacht sails is typical of thin wings operating at high Reynolds numbers (*Re*) and thin airfoil theory is able to predict most of the key flow features. The flow and pressure fields around sails have been investigated for decades with potential flow solvers [1] and in wind tunnels with smoke flow visualisation [2]. It is however only since the late 1990s [3] that, with the wider use of computational fluid dynamics, the viscous flow features, which are not modelled with potential flow theory, were solved and visualised on computer screens. For several years these numerical simulations have been *compared* with experimental force measurements showing differences of the order of 1%-10% [3,4]. We write *compared* instead of *validated* because experimental data have been typically compared with the results of one simulation, or a few simulations with different grids, while the validation of numerical simulations [5] requires a much wider investigation of the numerical error, known as *verification*, which unfortunately has rarely been performed in sail aerodynamics. Numerical simulations [6], where the uncertainty was rigorously assessed, showed that the grid uncertainty of typical grids used for RANS simulations in upwind sail aerodynamics is for say, the drag coefficient, about $\pm 0.5\%$ for the finest grids and $\pm 5\%$ for coarsest grids. It was found that the differences between numerical results and experimental data are mostly due to the difficulty of modelling the viscous flow features at the sharp leading edge (luff). It is therefore critical to enhance our understanding of these viscous flow features in order to improve our capability to predict the aerodynamic forces and, in turn, to enhance sail performance.

The current literature lacks detailed flow measurements of the flow around sails, such as particle imaging velocimetry or laser Doppler velocimetry data, and also there are no high-fidelity numerical simulations available, such as wall-resolved large eddy simulations. Therefore the near-wall flow field is still not well understood. On the other hand, in recent years, surface pressure measurements have been performed and have been used to estimate the correlated flow fields.

In light of some recent findings on the viscous flow features on sails [7,8], this paper aims to discuss further the pressure measurements that were published in 2011 by the same authors [9] on headsails. The original paper also includes a description of the measured pressures and expected flow field on the mainsail and a comparison between full scale and model scale. The pressure distributions presented herewith can be downloaded from www.ignazioviola.com.

2. METHOD

Global aerodynamic forces and pressure distributions were measured on model-scale rigid pressure-tapped sails, which were designed for the America's Cup class 'AC33'. A 1/15th-scale mainsail and headsail were built as fibreglass sandwich structures (Fig. 1) for the wind tunnel tests.

The core was made of a 2-mm-thick polypropylene plastic sheet, which had 3-mm-wide core flutes. Pressures were carried along the sail in the core-flutes to the sail foot. Pressure tubes carried the pressure from the sail foot to the transducers, which were placed in the cockpit. The transducers have a pressure range of ±450 Pa and a resolution of 9.25 mV/Pa.

The sails were perforated along four horizontal sections. On the four headsail sections, 7, 8, 11 and 15 holes were used on the top to the bottom sections, respectively. To measure the leeward side of the sail, tape was used to

[1] Lecturer, Institute for Energy Systems, School of Engineering, The University of Edinburgh, UK
[2] Professor, Yacht Research Unit, Department of Mechanical Engineering, The University of Auckland, NZ

close the holes on the windward side, and vice versa. In order to correctly model the leading edge (LE) flow field, the sails were chamfered at about 20° on the windward side to produce a sharp LE.

The sails were fixed onto a model-scale yacht with a rigid mast, and were tested in the Yacht Research Unit Wind Tunnel. The wind tunnel is an open jet with a test section 7 m wide and 3.5 m high.

Four different mainsail and headsail trims, four apparent wind angles (AWA), 16°, 20°, 24° and 28°, several heel angles and several twists of the onset flow were tested. The results presented and discussed in the paper are restricted to those measured in upright sailing conditions and with no twist in the onset flow.

The reference static pressure, p_∞, was provided by the static tap of a Pitot-static tube, which was located approximately at the same height as the top of the mast and 6 h upstream of the model (where h = 2.3 m is the model height). The difference between the total pressure tap and the static tap of the same Pitot-static tube was used to measure the reference dynamic pressure q_∞ = 32.5 Pa. The Reynolds number, *Re*, based on the average chord length, c = 0.49 m, was $Re = 2.3 \cdot 10^5$. The pressure measurement accuracy was estimated to be about $\pm$0.5 Pa.

Figure 1: A photograph of the wind tunnel test, looking upstream

3. RESULTS

The measured pressure distributions on the sail sections are related to the angle of attack (α), which resulted from the sail trims and the AWA. For each sail section, we call inviscid those flow features that could be predicted with potential flow (adopting the Kutta condition), and viscous those flow features that are due to the fluid viscosity. For example, the flow acceleration downstream of the stagnation point is a potential flow feature, while flow separation is a viscous flow feature.

The rest of this section is organised as follows: in §3.1 we present an overview of the pressures and flow field on the leeward side of the headsail; in §3.2 we describe the limiting condition where the stagnation point is at the LE; in §3.3 and §3.4 we describe the pressures and flow field for α higher and lower, respectively, than this limiting condition. Pressures and flow fields on the windward side of the sail are discussed in §3.5 and the effect of the mainsail trim on the headsail is discussed in §3.6.

3.1 Leeward side: overview

The pressure distribution along a sail section due to inviscid flow can be interpreted as the sum of the pressure distribution on a flat plate at incidence and the pressure distribution on a curved plate at the ideal angle of attack (α_0), i.e. when the local flow is tangent to the sail at the LE. This is shown schematically in Fig. 2, where the top row shows the sum of the geometrical configurations and the bottom row shows the sum of the pressure distributions on the upper side of the body.

The pressure coefficient is defined as: $C_p = (p - p_\infty)/\, q_\infty$. The C_p of a flat plate at incidence is infinitively low at the LE and deceases to zero towards the trailing edge (TE). Conversely, on a curved plate at incidence, $C_p = 0$ at the edges and is negative in between. The sum of the two pressure distributions leads to the typical pressure curve of thin highly curved foils with a suction peak near the LE and a suction peak near the maximum camber of the sail. The red dotted line in Fig. 2 shows how this pressure distribution is modified due to viscous flow features. Near the LE, the flow separates forming the laminar separation bubble (LSB), thus limiting the suction peak to a finite value. The LSB is discussed in detail in §3.3(b). Near the TE, the boundary layer (BL) separates leading to a low pressure gradient forming a plateau. The TE separation is discussed in detail in §3.3(f).

This schematic representation shows that the first suction peak, near the LE, is mostly correlated with α, while the second suction peak is mostly correlated with the sail curvature. The black dotted lines in Fig. 3 show how the pressure distributions are modified by an increase in α. Due to the orientation of the local normal-to-the-surface vector with respect to the sailed course, the pressure forces near the LE, which are mostly associated with the first suction peak, have a larger effect on the drive force than the pressure forces near the TE. Therefore a change in α has a larger effect on the drive force than on the side force. Conversely, the pressure forces on the rear part of the sail, that are mostly associated with the second

suction peak, have a larger effect on the side force than the pressure forces near the LE. Therefore a change in the sail curvature has a larger effect on the side force than on the drive force.

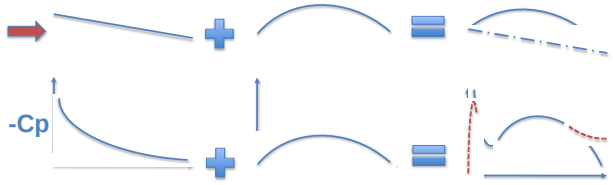

Figure 2. Schematic diagram of the pressure distributions on a sail section as a combination of a flat plate at $\alpha > \alpha_0$ and a curved plate at $\alpha = \alpha_0$

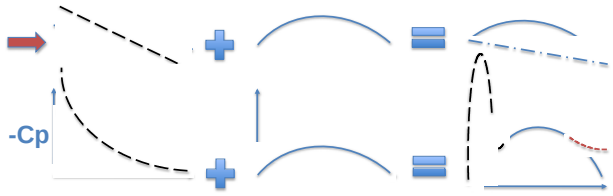

Figure 3. Schematic diagram of the pressure distributions illustrating the effect of an increase in α

Figure 4 shows schematic diagrams of the anticipated streamlines around horizontal headsail sections trimmed at different α. C_p plotted against the corresponding non-dimensional chords x/c are also shown. In particular, Figures from 4A to 4D show how the flow and pressure distributions vary with increasing α. In the following sections, firstly we discuss the condition $\alpha = \alpha_0$ (§3.2, Fig. 4B), then we discuss the condition $\alpha > \alpha_0$ (§3.3, Figs. 4C, 4D), and finally we discuss the condition $\alpha < \alpha_0$ (§3.4, Fig. 4A).

Figure 5 shows C_p measured on the mid-height section of the model-scale headsail at four different AWA: 16°, 20°, 24° and 28°. The pressure distribution at AWA = 20° corresponds to α_0 and to the flow field shown in Fig. 4B. Similarly, the pressure distributions at 16°, 24° and 28° can be related to the flow field shown in Figures 4A, 4C and 4D respectively.

3.2 Leeward side: $\alpha = \alpha_0$

The maximum drive force is typically achieved when the headsail is trimmed at, or slightly higher than α_0. Figure 4B shows the streamlines around the headsail section at $\alpha = \alpha_0$. The stagnation point is located at the LE. If the sail were flexible, this condition would lead the luff to collapse.

It should be noted that on a sail section there might not be a proper stagnation point with $C_p = 1$ because there might be a cross-flow component along a three-dimensional sail span. However, there must be one point on the sail where all the flow components are equal to zero and thus $C_p = 1$, but it does not have to occur on all the sail sections.

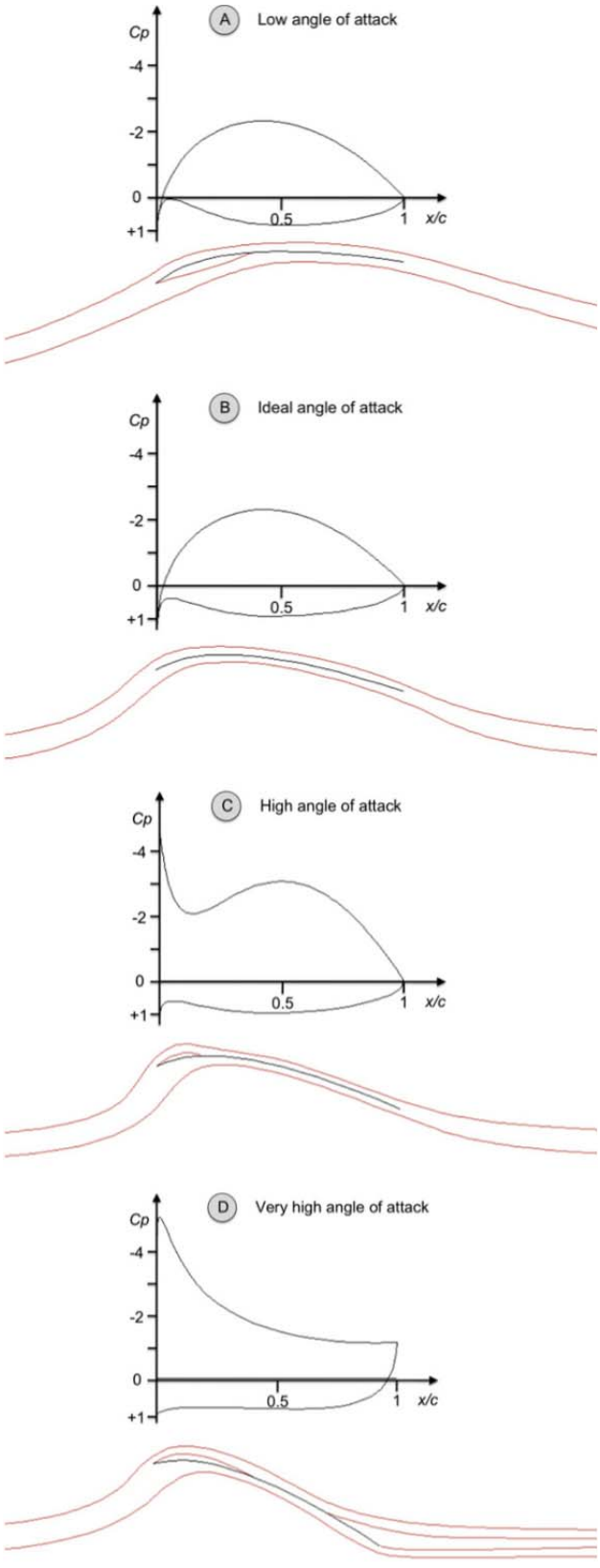

Figure 4. Schematic diagram of the expected flow fields for the typically measured C_p curves at five angles of attack (from ref. [9])

When $\alpha = \alpha_0$, an attached BL grows from the LE on both sides of the sail. The sail curvature leads to suction and pressure peaks on the leeward and windward sides respectively, related to the position of maximum camber. At the TE, $C_p \approx 0$ or is slightly negative.

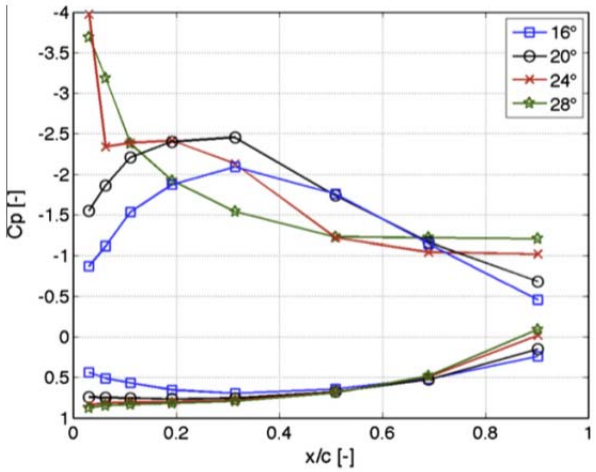

Figure 5. Measured leeward and windward C_p on the model-scale headsail along the mid-height section (from ref. [9])

3.3 Leeward side: $\alpha > \alpha_0$

3.3(a) Leading edge

The stagnation point is theoretically exactly at the LE only at $\alpha = \alpha_0$. Indeed, practically, the stagnation point is almost at the LE for a wide range of α around α_0. For instance, on a flat plate [10], α_0 occurs when the plate is aligned with the far-field wind direction ($\alpha = 0°$). However, it was found that the stagnation point is at the LE for $-20° < \alpha < 20°$. In ref. [10], the authors explained this finding by stating that: 'Although the LE appears to be sharp, it clearly must have thickness and be somewhat rounded'.

On the windward side, a BL grows along the short distance between the stagnation point and the LE. The pressure at the stagnation point is maximum (equal to the far field dynamic pressure) while it is very low at the LE (cf. the infinitely low LE pressure on a flat plate at incidence in potential flow), and therefore the BL must be laminar. At the LE, the laminar shear layer ejected from the windward side of the sail towards the leeward side is forced to turn abruptly downstream and instabilities lead to fast transition to turbulence. It is well known that the shape of the leading edge of delta wings, i.e. the direction of the flow at the separation point, has a significant effect on the shape of the LE vortex and, in turn, on the surface pressure distribution near the leading edge.

3.3(b) Laminar separation bubble (leeward side)

We assume that similarly to thin foils with a sharp leading edge, the turbulent transition on the separated shear layer leads to reattachment resulting in a closed streamline flow pattern, known as a laminar separation bubble (LSB). Vortices with a diameter of the order of the LSB thickness will be convected downstream and the instantaneous flow field will be made of a series of adjacent vortices along the sail surface. Most of these vortices will be rotating as if they were rolling on the surface. These vortices transport downstream the vorticity generated near the LE in the shear layer. The flow field is expected to be similar to the one presented in Figures 6A and 6B, which show the instantaneous spanwise vorticity and the time-averaged velocity, respectively, over an SD7003 foil at $Re = 60{,}000$ and $\alpha = 8°$ computed with quasi-3D LES [11].

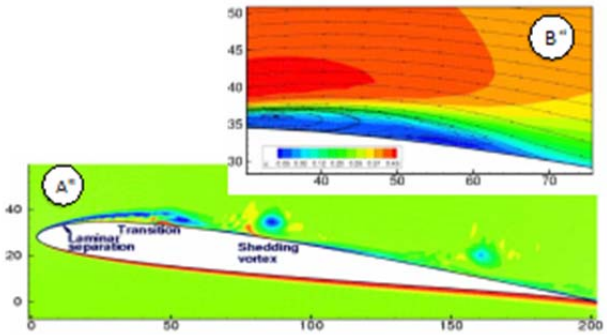

Figure 6. Instantaneous spanwise vorticity (A) and time-averaged velocity (B) over a foil with LSB (from ref. [11])

There are two types of LSB: short bubbles, which typically occur on rounded-nose conventional airfoils, and long bubbles, which typically occur at the sharp LE of thin foils such as sails.

The first bubble type is of particular interest in aeronautical applications. Laminar to turbulent transition occurs in the downstream-most part of the bubble, and the reverse flow velocity inside the bubble is typically less than 20% of the free-stream velocity [12]. Figure 7 shows a schematic diagram, which was drawn by Alam and Sandham [13], of the short LSB structure described by Horton [14].

The second LSB type became of interest in the 1950s, when high-speed aircraft adopted thin airfoils to decrease the effects of compressibility. Research on long bubbles also increased with the development of turbo-machinery and with the growth of low-*Re* aviation. The major characteristic of long bubbles is the generation of a large recirculation region with high backflow velocity. With long bubbles, separation occurs at the sharp LE and laminar to turbulent transition occurs at the upstream end of the bubble. An investigation of LSBs on flat plates performed at $Re = 2.13 \cdot 10^5$ shows that at least 95% of the shear layer is turbulent [10]. Consequently, reattached flow is more energetic from the long bubble type than from the short bubble type and the backflow in the recirculation region is significantly faster. The centrifugal force that curves the flow inside the bubble is due to a high suction inside the recirculation region. The backflow that decelerates near the LE can itself separate due to the high positive pressure gradient, forming a secondary separation bubble. Figure 8 shows a schematic

diagram of the long LE bubble type drawn by Crompton and Barret [10] on a flat plate at incidence.

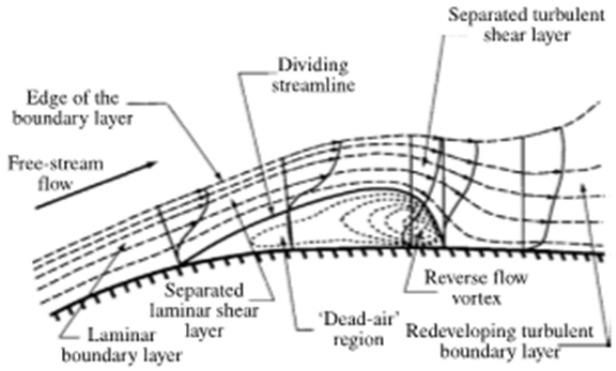

Figure 7. Schematic diagram of the short LSB type (from ref. [13])

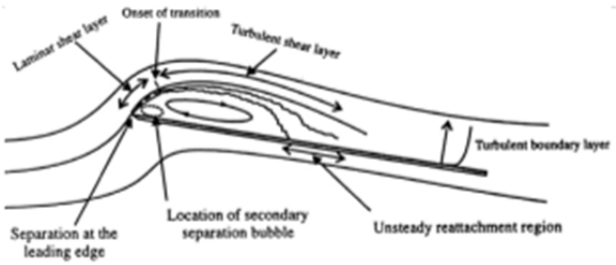

Figure 8. Schematic diagram of the long LSB type (from ref. [10])

3.3(c) Leading edge vortex

It is important to distinguish between the LSB, which occurs on upwind sails, and the leading edge vortex (LEV), which has been observed for the first time by Viola et al. [8] on downwind sails (Fig. 9). The LEV is a vortex that, like the LSB, is generated from the shear layer separated at the LE but, differently from the LSB, is not convected downstream and remains attached to the LE. Therefore near the LE there is a constantly high swirl velocity which is correlated with low pressure and whose circulation can contribute significantly to the overall lift of the sail. The LEV on downwind sails is a highly three-dimensional flow feature, which increases in diameter from the foot to the head where it merges with the tip vortex. Streamlines show a concentric spiral converging toward the centre of the vortex and increasingly deflected upwards toward the tip. While in the LSB the vorticity generated at the LE is convected downstream along the reattached BL, in the LEV the vorticity is convected toward the centre of the vortex and then extracted from vortex axial velocity, leading a much lower level of vorticity in the reattached BL. As a consequence, while the LSB is typically an undesirable flow feature that leads to low surface pressure gradients, the LEV can enhance the suction near the LE and thus it is an effective means to generate drive force.

The LEV occurs on a wide range of geometries and *Re*, from laminar flow conditions to fully turbulent flow conditions. It is the main lift generator in insect wings, bird hand-wings, and delta wings; it is the main source of extra lift in pitching foils, such as in helicopter blades; it can occur also on the sharp edges of bluff bodies such as buildings. The conditions that promote the formation of the LEV, instead of a LSB, are still unclear and the object of on-going research. However it is known that a high sweep angle and spanwise twist can promote the formation of the LEV. This explains why the LSB occurs on upwind headsails while the LEV occurs on highly swept and twisted downwind sails.

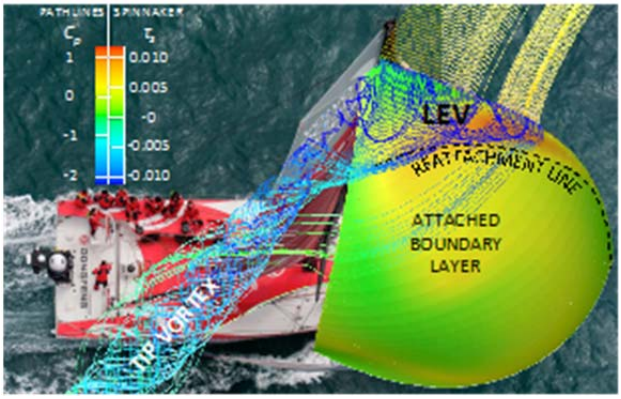

Figure 9. Over-impression of the LEV computed by Viola et al. [8] on a photograph of a yacht sailing downwind.

3.3(d) First suction peak

On headsails, the maximum suction peak is very close to the LE. Indeed, in the potential flow solution, $C_p = -\infty$ at the LE. The presence of the LSB moves the maximum suction peak somewhere downstream. For instance, on a flat plate, where the long-type LSB occurs, the suction peak has $C_p \approx -1$ at around 30% of the bubble length. The bubble length depends on α.

On a sail section, the minimum C_p is often lower than -4 and it is very close to the LE. Since $C_p = 1$ at the stagnation point, which is very close to the LE on the windward side, the resulting C_p is almost discontinuous at the LE. In the present paper, the distances of the closest pressure taps from the LE and the TE (located at roughly 3% and 98% of the chord, respectively) do not allow the LE and the TE pressures to be measured on either side.

Downstream of the suction peak, C_p increases at a high rate. The closer α is to α_0, the more positive the resulting gradient of C_p. For instance, on the windward side of a flat plate [10], the pressure increases monotonically up to the TE. At $\alpha = 1°$, C_p increases from $C_p = -1$ to $C_p \approx -0.2$ in the first 3% of the chord length, then it increases at a low rate until the TE where $C_p \approx -0.1$. At $\alpha = 5°$, C_p increases from $C_p = -1$ to only $C_p \approx -0.65$ in the first 3%. On a sail section, the pressure increases asymptotically reaching $C_p \approx -0.1$ at the TE.

Reattachment occurs downstream of the maximum pressure gradient, when $C_p \approx -0.3$. Differently from a flat plate, on a curved sail section it is not possible to

correlate exactly the maximum pressure gradient location downstream of the first suction peak with the reattachment point because the pressure gradient is also affected by the sail curvature. However numerical simulations [7] have shown that the reattachment point is indeed upstream of the maximum pressure recovery location and is somewhere near the maximum pressure gradient.

Increasing α causes the reattachment point to move further downstream, and the maximum positive pressure gradient decreases, leading to a smoother C_p curve.

3.3(e) *Re* effect on the first suction peak

Since the reattachment is driven by the laminar-to-turbulent transition, the LSB is particularly sensitive to *Re*. At low *Re*, the transition occurs later along the separated shear layer and thus reattachment is further downstream compared to high *Re*. Because the reattachment point is correlated with the maximum positive pressure gradient, the lower the *Re* the wider the LE suction peak. On the other hand, transition occurs in the separated shear layer, which is highly unstable, and therefore transition cannot be significantly delayed at low *Re*. As an example, on a flat plate [10], the reattachment point was found to be almost constant at $Re > 10^5$. This somewhat reassures us that wind tunnel tests, which are typically performed at one order of magnitude smaller that full-scale *Re*, should be able to reproduce the correct flow field. On the other hand, the said measurements on a flat plate were performed at a constant turbulence level of the onset flow. On full-scale sails, transition occurs almost certainly by a by-pass mechanism due to the high level of turbulence in the atmospheric BL. Therefore attention should be paid on how to scale the turbulent characteristics of the apparent wind onto sails in wind tunnels.

Additional considerations on the differences between pressure distributions measured on full- and model-scale upwind sails can be foun in refs. [15,16].

3.3(f) Second suction peak

Further downstream of the reattachment point, a curvature-related suction peak occurs. High sail curvature can lead to a high adverse pressure gradient and thus to TE separation. In these circumstances, the mean stream velocity and the velocity gradients in the separated region are small and hence, the pressure gradients downstream of the separation are small. Where separation occurs, the pressure recovery is interrupted, and the pressure remains almost constant at the so-called *base pressure* up to the TE.

As α increases, the LE bubble enlarges and the positive pressure gradient related to the reattachment decreases. The TE separation point moves upstream and, consequently, the curvature-related suction peak decreases. At very high α, the reduction of the positive pressure gradient and of the curvature-related suction peak leads to a monotonic pressure recovery from the LE suction peak to the base pressure (Fig. 4D).

At the TE of the headsail, the C_p is typically negative. In inviscid flow, at the TE, $C_p = 1$ for thick airfoils while $C_p = 0$ for infinitely thin profiles. Negative C_p's are related to separated flow.

At high α, when TE separation occurs on the leeward side of the sail, pressure recovery is interrupted by the separation process. Therefore, the higher the α, the lower the TE pressure. If TE separation does not occur, the C_p at the TE is typically in the range $-0.5 < C_p < 0$.

As α increases, the reattachment point moves downstream and the trailing edge separation point moves upstream and eventually these meet each other.

3.3(g) *Re* effects on the second suction peak

The trailing edge separation point is highly dependent on the Reynolds number. For instance, on a foil such as the NACA 653-618, stall occurs when the trailing edge point reaches the leading edge. The maximum lift is generated for α near but lower than the stall angle. For this foil, the maximum lift may increase by more than 20% when the Reynolds number increases from 3 million to 9 million [17]. Therefore, it is expected that the Reynolds number may significantly affect the pressure distribution near the TE, more than near the LE. In particular, the higher the Reynolds number, the higher the second suction peak.

3.4 Leeward side: $\alpha < \alpha_0$

On flexible headsails, when $\alpha < \alpha_0$, the LE collapses. Conversely, on rigid sails, the sail shape does not change. In this latter case, decreasing the α causes a LE bubble to occur on the windward side of the sail, and the camber-related suction and pressure peaks on the leeward and windward sides, respectively, to decrease (Fig. 4A).

3.5 Windward side

Figure 10 shows the windward C_p measured on the mid-height section of the model-scale headsail, for four different headsail trims and two AWA's. Trim 'J2' at AWA= 16° shows a pressure distribution typical of $\alpha = \alpha_0$. As the headsail is tightened (from 'J4' to 'J1') and also when the AWA is increased (from 16° to 28°), α increases.

For $\alpha > \alpha_0$, the stagnation point is on the windward side and the BL is attached up to the TE. At the LE, $C_p \approx 1$ and then decreases suddenly to lower values. The pressure gradients on either side of the stagnation point are so high that it is very difficult to measure the stagnation pressure due to the finite spacing between pressure taps. Downstream towards the trailing edge, the sail curvature causes the C_p to increase again. Finally, near the TE, C_p drops down to match the C_p on the leeward side. Therefore, the windward C_p shows a LE pressure peak (at the stagnation point) and a curvature related pressure peak.

Increasing α causes the suction peak to decrease, while the curvature-related pressure peak increases. The higher the α, the further upstream the pressure peak occurs (e.g.

see the curve for J1-16°). At high α, the LE suction peak becomes negligible and the pressure decreases monotonically up to the TE (e.g. see the curve for J1-28°, where $\alpha = 28°$ and the trim is tight).

On rigid sails, the sail shape does not change when $\alpha < \alpha_0$. In these circumstances, the stagnation point is on the leeward side and the LE separation bubble occurs on the windward side. Near the LE, $C_p \approx 1$ on the leeward side, while it is lower than 1 on the windward side where, downstream, C_p decreases further due to the LE bubble. The windward suction peak is smoother than the suction peak that occurs on the leeward side at $\alpha > \alpha_0$. This is probably due to the LE bubble being thicker due to the concave shape of the sail and having a lower backflow velocity. Downstream, C_p increases both due to reattachment and to sail curvature. The lower the α, the further downstream the reattachment occurs and, thus, the further downstream the positive pressure peak occurs (e.g. compare J3-16° and J4-16°).

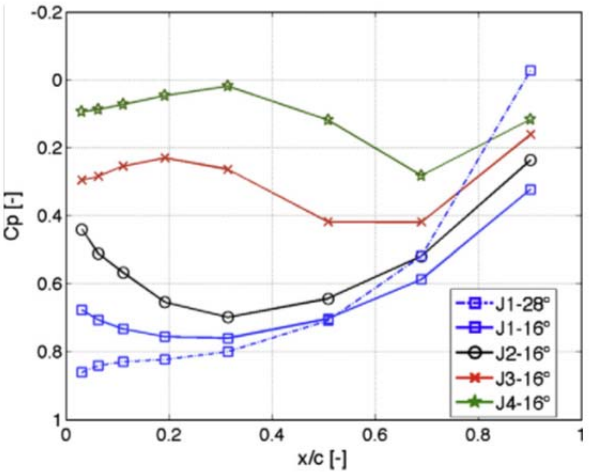

Figure 10. Measured windward *Cp* on the model-scale headsail along the mid-height section (from ref. [9])

3.6 Effect of the mainsail

The lift generated by the mainsail has two consequences on the headsail pressure distribution. Firstly, it causes α to increase for the headsail (upwash). In fact, when either the mainsail or the headsail is trimmed in, the measured pressure distribution trend on the headsail is similar. Secondly, the headsail TE pressure decreases due to the *'slot effect'* [1], because the TE is in the mainsail suction region. Therefore, if TE separation does not occur, increasing the AWA or trimming in the mainsail, causes a lower pressure on the leeward side of the mainsail, which leads to a lower headsail TE pressure, and thus to more suction along its entire leeward side.

4. CONCLUSIONS

We discussed wind tunnel surface pressure measurements on a model-scale headsail and we proposed a description of the correlated flow field near the sail based on analogies with other fluid flows. We showed that the general pressure field can be interpreted as the result of an inviscid flow field. Particularly, inviscid flow leads to two suction peaks and two pressure peaks on the leeward and windward side of the sail, respectively. The first peak is correlated with the angle of attack and the second peak is correlated with the sail curvature. On the other hand, viscous flow features dominate the pressure distributions in the regions near the leading and trailing edges. We propose that a long-type laminar separation bubble occurs at the leading edge, while trailing edge separation may occur for high angles of attack. The reattachment point of the bubble is near and upstream of the maximum positive pressure gradient downstream of the first suction peak. Increasing the angle of attack causes: the reattachment point to move downstream; the maximum positive pressure gradient to decrease and thus the first suction peak to be smoother; the trailing edge suction peak to move upstream and thus the second suction peak to be smoother. The reattachment point is more likely to be sensitive to the onset flow turbulence than to the Reynolds number, which, on the contrary, could significantly vary the point of separation near the trailing edge at high angles of attack.

We think that the detailed description of the flow field near yacht sails that has been presented in the paper will allow a deeper understanding of sail pressure distributions and, therefore, of the aerodynamic forces experienced by sailing yachts in upwind conditions.

Acknowledgements

This project has received funding from the European Union's Seventh Programme for research, technological development and demonstration under grant agreement No PIRSES-GA-2012-318924 (SAILING FLUIDS) and from the Royal Society of New Zealand.

References

1. Gentry, A.E. (1971), "The Aerodynamics of Sail Interaction", *Proc. of the 3rd AIAA Symposium on the Aero/Hydronautics of Sailing*, Redondo Beach, CA, Nov.
2. Marchaj, C. A., & Barker, S. (1964), *Sailing theory and practice*, Adlard Coles.
3. Miyata, H., & Lee, Y. W. (1999), "Application of CFD Simulation to the Design of Sails". *Journal of Marine Science and Technology*, **4**(4), 163-172.
4. Querard, A. B. G., & Wilson, P. A. (2007), "Aerodynamic of modern square head sails: a comparative study between wind-tunnel experiments and RANS simulations", *International Journal of Small Craft Technology*, **147**(B1).
5. ASME (2009), *V&V 20: Guide for Verification and Validation in Computational Fluid Dynamics and Heat Transfer*, ISBN/PUB: C07309.

6. Viola, I. M, Bot, P. & Riotte, M. (2013), “On the uncertainty of CFD in sail aerodynamics”, *International Journal for Numerical Methods in Fluids*, **72**(11), 1146-1164.

7. Viola, I. M., Bot, P. & Riotte, M. (2013), “Upwind sail aerodynamics: A RANS numerical investigation validated with wind tunnel pressure measurements” *International Journal of Heat and Fluid Flow*, **39**, 90-101.

8. Viola, I. M., Bartesaghi, S., Van Renterghem, T. & Ponzini R. (2014, 1 Nov), “Detached Eddy Simulation of a Sailing Yacht”, *Ocean Engineering*, **90**, 93–103.

9. Viola, I. M. & Flay, R. G. J. (2011), “Sail aerodynamics: understanding pressure distributions on upwind sails”, *Experimental Thermal and Fluid Science*, **35**(8), 1497-1504.

10. Crompton, M. J., Barret, R. V. (2000), “Investigation of the separation bubble formed behind the sharp leading edge of a flat plate at incidence”, *Proc. Inst. of Mech. Eng., Part G: J. of Aerospace Eng.*, **214**(3), 157-176.

11. Yuan, W., Xu, H., Khalid, M., & Radespiel, R. (2006), “A parametric study of LES on laminar-turbulent transitional flows past an airfoil”, *International Journal of Computational Fluid Dynamics*, **20**(1), 45-54.

12. Gault, D.E. (1957), “An investigation at low speed of the flow over a simulated flat plate at small angles of attacks using Pitot static and hot wire probes”, NACA TN-3876.

13. Alam, M., Sandham N.D. (2000), “Direct numerical simulation of ‘short’ laminar separation bubbles with turbulent reattachment”. *J. Fluid Mech.*, **410**, 1–28.

14. Horton, H. P. (1968), “Laminar separation in two and three-dimensional incompressible flow”. PhD Dissertation, University of London.

15. Viola, I. M. (2013), “Recent advances in sailing yacht aerodynamics”, Applied Mechanics Reviews, **65**(4), 040000, 1-12.

16. Viola, I. M. & Flay, R. G. J. (2011), “Sail pressures from full-scale, wind-tunnel and numerical investigations”, *Ocean Engineering*, **38**(16), 1733-1743.

17. Abbott, I. H., Von Doenhoff, A. E. (1959), *Theory of wing sections, including a summary of airfoil data*, Dover Publications, Inc., New York